IEEE Access
Multidisciplinary | Rapid Review | Open Access Journal

Received April 27, 2020, accepted May 8, 2020, date of publication May 12, 2020, date of current version May 26, 2020.

Digital Object Identifier 10.1109/ACCESS.2020.2994128

Numerical Study for Zero-Power Maglev System Inspired by Undergraduate Project Kits

ZEYI ZHANG, TAO GAO, YAO QIN, JIE YANG, AND FAZHU ZHOU
School of Electrical Engineering and Automation, Jiangxi University of Science and Technology, Ganzhou 341000, China

Corresponding author: Jie Yang (yangjie@jxust.edu.cn)

This work was supported in part by the National Natural Science Foundation of China under Grant 61763016, and in part by the High-level Talents Research Start-up Project of Jiangxi University of Science and Technology under Grant 205200100476.

ABSTRACT The single-axis maglev system is increasingly popular as undergraduate project kits over the recent years. Though it is simple and instructive, the large current in the electromagnet leads to the overheating problem. In order to enhance the energy-saving performance as well as the controller performance, this work compares three geometric modifications on the iron core, the upper permanent magnet and the floating permanent magnet for the maglev system. Four target cases are defined to incorporate the geometric modifications and are solved numerically. Moreover, the numerical solutions are carefully analyzed in terms of the zero-power force, the controller-gain requirement and the saturation current. Consequently, two approaches, i.e., extending the iron core and enlarging the floating magnet, can improve both the zero-power force and the controller-gain requirement and are highly recommended for the zero-power maglev system. On the contrary, though the upper magnet can improve the zero-power force, it significantly raises the controller-gain requirement and accelerates the saturation of the iron core.

INDEX TERMS Zero-power maglev, electromagnetic suspension, permanent magnets, numerical simulation.

I. INTRODUCTION

The electromagnetic suspension (EMS) technology has become an intensive research topic for the railway transportation in Germany, Japan, and China since 1960s [1]. Apart from the transportation, the maglev technology can also contribute to frictionless bearing [2], vibration isolation for semiconductor industry [3], levitation of metal slabs during manufacture [4], etc.

Due to its nonlinear dynamics, open-loop instability, and simplicity, the single-axis maglev system attracts great attention in terms of the controller design for the undergraduate education [2], [4]–[6]. In 1986, Wong [5] designed an analog maglev control system as an undergraduate project. Specifically, the optical distance sensor was used to measure the floating distance of the floater, whereas the current in the electromagnet was adjusted by the analog controller accordingly in order to maintain a stable floating distance. In 1989, Oguchi and Tomigashi [2] proposed to incorporate the digital controller for the single-axis maglev system. Based on the digital controller, Cho *et al.* [3], Barie and Chiasson [4], Hajjaji and Ouladsine [7], Yu and Li [8], and Hernandez-Casanas *et al.* [9] implemented different advanced control algorithms on the undergraduate project kits, including sliding-mode control, nonlinear state-space control, and fuzzy control. Moreover, Hurley and Wolfle [6] optimized the geometric design of the electromagnet for the maglev kit with the finite element analysis. Nevertheless, Lundberg *et al.* [10] and Yoon and Moon [11] simplified the kit design by replacing the optical distance sensor with the hall-effect sensor to measure the distance between the magnetic floater and the electromagnet. Recently, GOOGOLTECH® [12] launched the commercial undergraduate project kit, GML2001, with the ferrimagnetic ball as the floater, as shown in Fig. 1(a).

However, the single-axis maglev system may be overheated due to the large current in the electromagnet [6], which in turn influences the resistance and inductance of the electromagnet [7] as well as the performance of the controller. Such overheating problem also occurs in the EMS transportation system and leads to the study on the hybrid permanent-electromagnetic suspension (PEMS) technology [1], which incorporates the permanent magnet within the electromagnet. Wang and Tzeng [13] attached the permanent magnets to

The associate editor coordinating the review of this manuscript and approving it for publication was Gerardo Di Martino.

the top of the iron core. Zhang *et al.* [14] further proposed a new configuration to insert the permanent magnet into the iron core and compared its zero-power performance with the conventional EMS configuration by numerical simulation. Nevertheless, the permanent-magnetic suspension (PMS) technology demonstrated the outstanding zero-power performance [15].

Inspired by the undergraduate maglev kit and the PEMS technology, there are generally three approaches to realize a zero-power maglev system,

- Optimizing the iron core of the electromagnet to minimize the magnetic reluctance [2], [6], [8], [9];
- Attaching the permanent magnet to the electromagnet [1], [13], [14];
- Using the floating magnet and enlarging its size [3], [7], [10], [11].

However, besides the energy-saving incentive, few attentions were paid to the side-effects on the controller design by those geometric modifications of the zero-power maglev system. This work aims to further explore the physical mechanism for the zero-power maglev system from the following three aspects:

- Zero-power force: indicating loading ability;
- Controller-gain requirement: indicating hardware specification;
- Saturation current: indicating working range.

This work utilizes the numerical simulation by ANSYS® [3], [9], a commercial software, to solve for magnetic fields and forces. Meanwhile, parametric studies on the excitation current and the geometric parameters are carried out to understand their respective roles in the zero-power control.

This work is organized as follows. Sec. II elaborates the methodologies applied in this work, including the physical modelling and the simulation modelling. In particular, four target cases are defined in Sec. II.A.1 for the comparison among the core extension, the upper magnet, and the floating magnet. In Sec. III, the solutions of the four cases are carefully analyzed in terms of the zero-power control. Moreover, the transitions from Case 0 to the other three cases are respectively discussed Sec. III.C. Finally, concluding remarks are addressed in Sec. IV.

II. METHODOLOGY

A. PHYSICAL MODELLING

1) BASIC STRUCTURE

Generally, the zero-power maglev system is axial symmetric as shown in Fig. 1(b) and mainly consists of four components, including the coil, the iron core, the upper magnet, and the floating magnet. The z-axis is along the centerline of the iron core and its origin locates on the lower surface of the iron core. Also, Fig. 1(b) labels out the geometries of each component, as summarized in Table 1. Note that the additional load can be attached to the floating magnet. Besides, the floating distance, Z_h, is kept as a constant in this work.

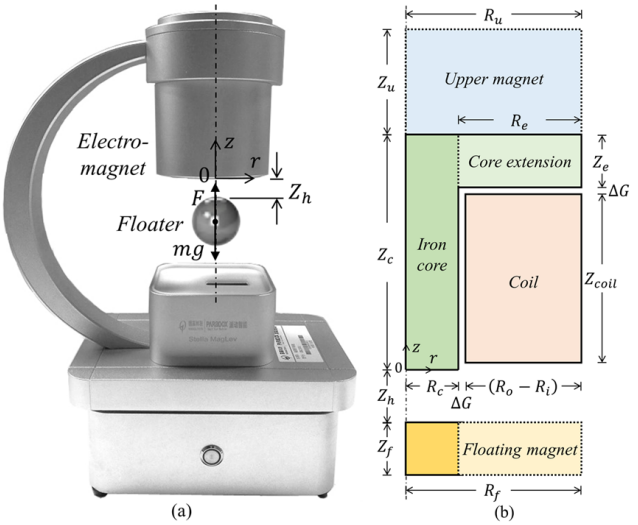

FIGURE 1. (a) A typical single-axis maglev system as the commercial undergraduate project kit by GOOGOLTECH® [12] and (b) the axial-symmetric geometry of the zero-power maglev system with the origin of the z-axis located on the lower surface of the iron core.

TABLE 1. Geometries of the single-axis maglev system.

Symbol	Quantity	Value (mm)
Z_u	Upper magnet thickness	0 to 30
R_u	Upper magnet radius	50
Z_c	Core height	67
R_c	Core radius	15
Z_e	Core-extension thickness	15
R_e	Core extension	0 to 35
ΔG	Gap	2
Z_{coil}	Coil height	48
R_i	Coil inner radius	17
R_o	Coil outer radius	50
Z_h	Floating distance	15
Z_f	Floating magnet thickness	15
R_f	Floating magnet radius	15 to 50

In order to understand the respective roles of the core extension, the upper magnet, and the floating magnet in the zero-power control, there are three geometric variables listed in Table 1,

- The core extension, R_e, varying from 0 to 35 mm;
- The upper magnet thickness, Z_u, varying from 0 to 30 mm;
- The floating magnet radius, R_f, varying from 15 to 50 mm.

Moreover, four target cases are defined in Table 2. Case 0 is regarded as the benchmark, whereas Cases 1, 2, and 3 with modified geometries are to be compared with Case 0. Specifically, Case 1 removes the core extension, Case 2 adds a large upper magnet, and Case 3 enlarges the floating magnet.

The iron core uses the cold-rolled steel, whose characteristic magnetization ($B - H$) curve is tabulated in Table 3. Hence, the cold-rolled steel gets magnetically saturated around 1.90 T.

TABLE 2. Geometric parameters of four target cases.

Case	R_e	Z_u	R_f	Description
0	35	0	15	Benchmark
1	0	0	15	No core extension
2	35	30	15	Large upper magnet
3	35	0	50	Larger lower magnet

TABLE 3. Magnetization ($B-H$) curve of the cold-rolled steel.

H (A/m)	B (T)
0	0.00
1080	0.858
1480	1.06
2090	1.26
3120	1.44
5160	1.61
9930	1.77
15500	1.86
25000	1.88
35000	1.90

Both the floating magnet and the upper magnet use the neodymium magnet of Grade N35, whose relative permeability is $\mu_r = 1.05$ and magnetic coercivity is $H_c = -9.47 \times 10^5$A/m. Moreover, the two magnets have the same upward orientation.

The coil uses the copper and consists of tightly-packed windings with N turns. Denote the current in the windings as i, and the excitation current, I, can be expressed as,

$$I = Ni. \tag{1}$$

Moreover, as a sign convention, the magnetic field in the iron core excited by a positive excitation current has the same upward orientation as the floating magnet.

2) ZERO-POWER LINEAR APPROXIMATION

Denote the magnetic force on the floating magnet as F, which can be expressed as a function of the excitation current and the floating distance [11],

$$F = F\left(I, Z_h\right), \tag{2}$$

where F increases as the increase of I, i.e., $\partial F/\partial I > 0$, and decreases as the increase of Z_h, i.e., $\partial F/\partial Z_h < 0$ [6].

When $I = 0$A, the coil does not excite any magnetic field, but the floating magnet still magnetizes the iron core and gets attracted, i.e., $F \neq 0$. Hence, denote the non-zero magnetic force on the floating magnet when $I = 0$ A as the zero-power force, F_0.

When the floating distance is fixed and the excitation current changes by a small amount, i.e., $\Delta Z_h = 0$ and $\Delta I = I - 0$ A, the magnetic field excited by the coil is superposed with the magnetic fields excited by magnets insides the iron core. The zero-power linear approximation assumes that the magnetic flux density within the iron core is much smaller than the saturation limit, i.e., $B \ll 1.9$T. Hence, within the linear regime, the change of the magnetic force, i.e., $\Delta F = F - F_0$, is proportional to ΔI in the form of,

$$\Delta F = k_{linear}\,\Delta I, \tag{3}$$

where k_{linear} is named as the linear-approximation coefficient.

Moreover, denote the change of the magnetic flux density in the iron core due to ΔI as ΔB. By applying the Ohm's law of the magnetic field, ΔB can be expressed as,

$$\Delta B \propto \Delta I/R_m, \tag{4}$$

where R_m is the effective magnetic reluctance for the combination of the iron core and the surrounding air gap. Hence, Cases 0, 2, and 3 share the same R_m, while Case 1 has a larger R_m due to the smaller iron core and the increased air gap.

Furthermore, because the magnetic field can be linearly superposed within the linear regime, ΔF is proportional to ΔB and can be expressed as,

$$\Delta F = k_B \Delta B, \tag{5}$$

where the sensitivity coefficient k_B corresponds to the degree of interaction between the floating magnet and the iron core. Hence, Cases 0 and 2 share the same k_B due to the same sizes of the floating magnet and the iron core. Case 1 has a smaller k_B than Case 0 due to the smaller iron core, while Case 3 has a larger k_B than Case 0 due to the larger floating magnet.

By combining (3), (4), and (5), we can derive the following relationship under the zero-power linear approximation,

$$k_{linear} = \Delta F/\Delta I \propto k_B/R_m. \tag{6}$$

Nevertheless, Table 4 outlines the change of k_{linear} with respect to geometric modifications on R_e, Z_u, and R_f. Hence, by referring to Table 4, Cases 0 and 2 share the same k_{linear}. Case 1 has a smaller k_{linear} than Case 0, while Case 3 has a larger k_{linear} than Case 0.

TABLE 4. Influences on R_m, k_B, and k_{linear} by geometric modifications.

Geometry Modification	R_m	k_B	k_{linear}
Decreasing R_e	↗	↘	↘
Increasing Z_u	→	→	→
Increasing R_f	→	↗	↗

3) STABILITY ANALYSIS

At the equilibrium, the magnetic force is equal to the floating load denoted as G, which gives,

$$F = G. \tag{7}$$

In order to evaluate the stability of the zero-power maglev system, denote the restoring stiffness as k_{stiff}, which can be expressed as,

$$k_{stiff} = \frac{dF}{dZ_h} = \frac{\partial F}{\partial I}\frac{\partial I}{\partial Z_h} + \frac{\partial F}{\partial Z_h}, \tag{8}$$

where $\partial F/\partial I$ equals to k_{linear} within the linear regime.

If I is kept as a constant, i.e., $\partial I/\partial Z_h = 0$, the restoring stiffness is negative, i.e., $k_{stiff} = \partial F/\partial Z_h < 0$ [6]. In reality, there are disturbances acting on the floater, such as wind or vibration. Assuming the disturbance drags down the floater, i.e., $\Delta Z_h > 0$, the magnetic force reduces by $|k_{stiff}\Delta Z_h|$ and becomes smaller than the floating load, i.e., $F < G$, which further accelerates the floater to deviate from the equilibrium. Consequently, the equilibrium with a negative restoring stiffness is unstable [6].

Moreover, in order to realize a stable equilibrium with a positive resorting stiffness, the active controller [11] is applied to adjust the current output according to the floating-distance input, i.e., $\partial I/\partial Z_h > 0$. Since $k_{linear} > 0$ and $\partial F/\partial Z_h < 0$, the stability criterion within the linear regime, i.e., $k_{stiff} > 0$, can be derived from (8),

$$\frac{\partial I}{\partial Z_h} > -\frac{\partial F}{\partial Z_h}\Big/ k_{linear}, \tag{9}$$

where $\partial I/\partial Z_h$ represents the controller gain between the floating-distance input and the current output. Assuming the disturbance drags down the floater, i.e., $\Delta Z_h > 0$, in order to increase F and to reduce Z_h, I should increase by at least $|\Delta Z_h (\partial F/\partial Z_h)/k_{linear}|$ so that the equilibrium becomes stable.

Technically, the change of the current is restricted by the hardware specifications, such as the power supply and the coil induction. Hence, the current is difficult to be adjusted by a large amount in a short time. Consequently, a small controller gain is preferred for the ease of control, i.e., $\min(\partial I/\partial Z_h) = [-(\partial F/\partial Z_h)/k_{linear}]$.

Furthermore, the magnitude of $\partial F/\partial Z_h$ generally increases as the increase of F_0 [6], [11]. However, the relationships between $\partial F/\partial Z_h$ and geometric modifications as well as the ratio between $\partial F/\partial Z_h$ and k_{linear} are not straightforward due to the nonlinearity in the magnetic force. Hence, in order to clarify the controller-gain requirement, i.e., $\min(\partial I/\partial Z_h)$, this work utilizes the numerical simulation to solve for $\partial F/\partial Z_h$.

4) SATURATION APPROXIMATION

When I exceeds a certain critical value, I_{sat}, the iron core would get saturated as the magnetic flux density increases over 1.9T. The saturation approximation assumes that the iron core is saturated and its relative permeability approaches the unity. Hence, the change of the magnetic force, i.e., $\Delta F = F_1 - F_2$, is proportional to the change of the current, i.e., $\Delta I = I_1 - I_2$, in the form of,

$$\Delta F = k_{sat}\Delta I, \tag{10}$$

where k_{sat} is named as the saturation-approximation coefficient.

It is worth noting that due to the saturation in the iron core, k_{sat} will be much smaller than k_{linear}. Such a large change in the $F - I$ coefficients could lead to oscillation or even loss of control for the maglev system. Hence, I_{sat} indicates the feasible working range of the maglev system.

B. SIMULATION MODELLING

Due to the nonlinear permeability of the iron core and the distribution of the magnetic field in the air, it is difficult to solve for the magnetic force analytically. Hence, the maglev system is numerically computed by the 2D magneto-static solver in ANSYS®, with the following details,

- The cylindrical coordinate is applied and is axial-symmetric about the z-axis.
- In order to minimize the near-field error, a large vacuum space by $22R_o \times 32(Z_c + Z_u)$ is defined surrounding the maglev system. Also, the balloon boundary condition is applied to the boundary of the vacuum space.
- The material properties, such as the $B - H$ curve of the cold-rolled steel and the magnetic coercivity of the neodymium magnet, are manually defined in the solver.
- The convergence criterion is set to be 0.01% energy error, and the solver iteratively refines the adaptive mesh by 30% per pass until the convergence criterion is satisfied.

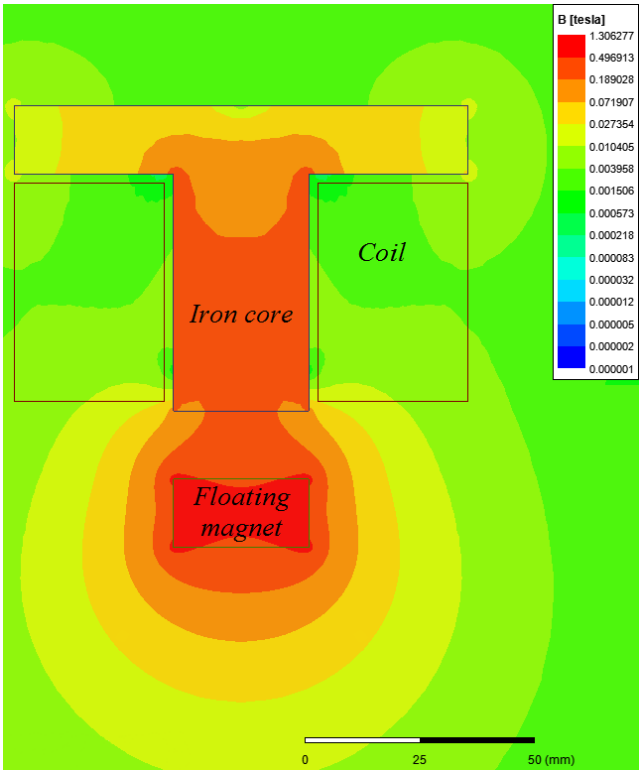

FIGURE 2. Magnetic field (magnitude of the magnetic flux density) around the maglev system of Case 0 with $I = 0$ A.

Fig. 2 shows the numerical result of Case 0 with $I = 0$A by the distribution of the magnetic field (*magnitude of the magnetic flux density*) around the maglev system. It takes 13 passes in total to meet the convergence criterion and the final number of mesh triangles is 6283. Moreover, the magnetic field excited by the floating magnet magnetizes the lower part of the iron core, and the magnetic force on the floating magnet is solved to be $F_0 = 9.17$ N.

III. RESULTS AND DISCUSSION

A. SOLUTION OF CASE ONE

The parametric study is conducted on Case 0 by varying the current from $I = -1.29\times10^3$A to 4.21×10^4A.

Fig. 3 shows the variation of the magnetic force on the floating magnet with respect to the current. The $F - I$ curve has two quasi-linear portions at the two ends, and bends around $I = 9.5\times10^3$A.

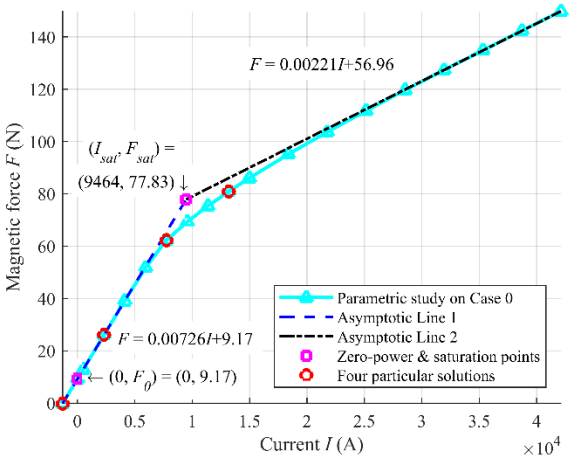

FIGURE 3. Parametric study on Case 0 by varying the current, including two asymptotic lines, the zero-power point, the saturation point and four particular solutions.

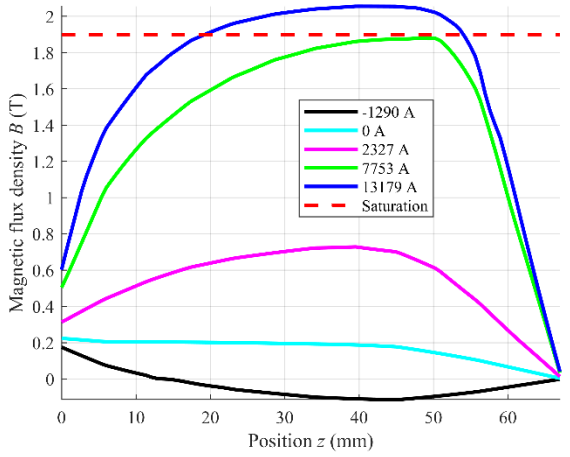

FIGURE 4. Magnetic flux density along the centerline of the iron core for five particular solutions of Case 0 with $I = -1290, 0, 2327, 7753,$ and 13179 A.

In order to understand the underlying mechanism of the bending in Fig. 3, four particular solutions with $I = -1290$, 2327, 7753, and 13179 A and the zero-power solution are selected for further examination. Fig. 4 shows the magnetic flux density, B, along the centerline of the iron core, $z \in [0, 67mm]$ and $r = 0$, for the five particular solutions of Case 0. It is observed that the magnetic flux density increases as the increase of the current. As mentioned in Sec. II.A.1, the cold-rolled steel is saturated at the magnetic flux density around 1.9 T. The $I = 7753$ A curve touches the saturation line with $B = 1.9$ T, whereas most part of the $I = 13179$ A curve exceeds the saturation line. Hence, the saturation of the iron core occurs between $I = 7753$ A and $I = 13179$ A. Consequently, the transition between the two quasi-linear portions in Fig. 3 corresponds to the saturation of the iron core.

Moreover, motivated by (3) and (10), we can derive two first-order asymptotic lines by the least-square method, as shown in Fig. 3. Specifically, Asymptotic Line 1, $F = 0.00726I + 9.17$, corresponds to the zero-power linear approximation, whereas Asymptotic Line 2, $F = 0.00221I + 56.96$, corresponds to the saturation approximation. So, the zero-power force is $F_0 = 9.17$N, the linear-approximation coefficient is $k_{linear} = 0.00726$N/A, and the saturation-approximation coefficient is $k_{sat} = 0.00221$N/A.

Furthermore, the saturation point is defined as the intersection between the two asymptotic lines, which gives $(I_{sat}, F_{sat}) = (9464, 77.83)$. Hence, the curve bends near the saturation point, and the slope of the curve drops from $k_{linear} = 0.00726$ N/A to $k_{sat} = 0.00221$N/A by around 70%. Such a strong nonlinear effect could lead to oscillation or even loss of control for the maglev system. Hence, I_{sat} indicates the feasible working range of the maglev system.

Nevertheless, according to the stability analysis in Sec. II.A.3, the maglev system is able to balance a floating load equal to F_0 with a zero current as long as the active restoring stiffness is positive. In (9), $\partial F/\partial Z_h$ at $Z = Z_{h0}$ is estimated by the central difference method and can be expressed as,

$$\left.\frac{\partial F}{\partial Z_h}\right|_{Z=Z_{h0}} \approx \frac{F|_{Z_h=Z_{h2}} - F|_{Z_h=Z_{h1}}}{2\Delta h}, \tag{11}$$

where the magnetic forces at $Z_{h1} = Z_{h0} - \Delta h$ and $Z_{h2} = Z_{h0} + \Delta h$ are numerically calculated and $\Delta h = 0.1$ mm is used in this work. Consequently, the two magnetic forces, $F|_{Z_h=14.9\text{mm}} = 9.2682$N and $F|_{Z_h=15.1\text{mm}} = 8.9828$N, lead to $\partial F/\partial Z_h|_{Z=15\text{mm}} = -1.43$N/mm and the controller-gain requirement, $\min(\partial I/\partial Z_h) = 197$A/mm.

TABLE 5. Parameters calculated from the $F - I$ curves of the four cases.

Case	F_0 (N)	k_{linear} (N/A)	I_{sat} (A)	F_{sat} (N)
0	9.17	0.00726	9464	77.8
1	7.60	0.00515	15969	89.9
2	43.55	0.00728	4392	75.5
3	53.60	0.0199	5153	156.3

B. SOLUTIONS OF FOUR CASES

Parametric studies are also conducted on Cases 1, 2, and 3 by varying the current, while the asymptotic lines for each case are derived. Moreover, Table 5 summarizes calculated parameters, including F_0, k_{linear}, I_{sat}, and F_{sat} for the four cases. From Table 5, we observe the following features:

- F_0 decreases for Case 1 due to the smaller iron core, whereas F_0 increases significantly for Cases 2 and 3 due

to the large upper magnet and the larger floating magnet, respectively.

- The changes of k_{linear} are consistent with the theoretical derivations in Table 4. In addition, k_{linear} of Cases 0 and 2 are almost equal, which is also observed in Fig. 7 of [14] for the PEMS system.
- I_{sat} increases for Case 1 due to the smaller iron core and the larger effective magnetic reluctance, R_m, in (4). Moreover, I_{sat} decreases for both Cases 2 and 3 due to the initial magnetization of the iron core by the floating magnet and the upper magnet, respectively. Hence, I_{sat} is determined by both the core extension and the initial magnetization.
- F_{sat} increases for Case 3, whereas F_{sat} of Cases 1 and 2 are close to that of Case 0. This phenomenon can be explained by the observation from Fig. 4. At $I = I_{sat}$, the magnetic fields in the iron core have similar magnitudes around 1.9 T for the four cases and may differ slightly in the distribution. Hence, F_{sat} is mainly determined by the floating magnet and the saturated iron core, rather than the core extension or the upper magnet.

Furthermore, it is worth comparing Case 2 and Case 3. Case 2 has a lower I_{sat} due to the contact between the upper magnet and the iron core, which greatly accelerates the saturation of the iron core. Also, Case 2 has a lower F_0 due to the transmission loss of the magnetic flux through the iron core. Consequently, the upper magnet enhances F_0 with a higher price of the saturation in the iron core than that of the floating magnet.

Nevertheless, Table 6 summarizes calculated parameters regarding the zero-power control for the four cases. As discussed in Sec. II.A.3, a small $\min\left(\partial I/\partial Z_h\right)$ is preferred for the ease of control. Hence, Case 3 outperforms the other three cases in terms of the largest zero-power force and the smallest controller-gain requirement, mainly due to its larger floating magnet and the larger degree of interaction, k_B.

TABLE 6. Parameters regarding zero-power control for the four cases.

Case	F_0 (N)	k_{linear} (N/A)	$\partial F/\partial Z_h$ (N/mm)	$\min(\partial I/\partial Z_h)$ (A/mm)
0	9.17	0.00726	-1.43	197
1	7.60	0.00515	-1.23	239
2	43.55	0.00728	-3.60	494
3	53.60	0.0199	-3.03	152

C. SOLUTIONS OF TRANSITIONS

In order to confirm the discussions regarding the zero-power control in Sec. III.B, this subsection discusses the transitions from Case 0 to the other three cases, respectively.

1) FROM CASE 0 TO CASE 1

Table 7 summarizes calculated parameters regarding the zero-power control when R_e decreases from 35 mm to 0 mm. From Table 7, we observe the following features:

TABLE 7. Parameters regarding zero-power control during transition from Case 0 to Case 1.

	R_e	F_0	k_{linear}	$\partial F/\partial Z_h$	$\min(\partial I/\partial Z_h)$
Case 0	35.00	9.17	0.0073	-1.43	197
	26.25	8.83	0.0066	-1.38	208
Transition	17.50	8.46	0.0062	-1.40	225
	8.75	8.03	0.0055	-1.29	235
Case 1	0.00	7.60	0.0052	-1.23	239

- As discussed in Sec. III.B, both F_0 and k_{linear} increase as the increase of R_e.
- The magnitude of $\partial F/\partial Z_h$ increases as the increase of F_0 [6], [11].
- Since the change of k_{linear} is larger than that of $\partial F/\partial Z_h$, $\min\left(\partial I/\partial Z_h\right)$ decreases as the increase of R_e.

Hence, the core extension enhances F_0 and reduces $\min\left(\partial I/\partial Z_h\right)$ simultaneously.

TABLE 8. Parameters regarding zero-power control during transition from Case 0 to Case 2.

	Z_u	F_0	k_{linear}	$\partial F/\partial Z_h$	$\min(\partial I/\partial Z_h)$
Case 0	0.0	9.17	0.0073	-1.43	197
	7.5	20.74	0.0069	-2.16	312
Transition	15.0	29.98	0.0074	-2.79	376
	22.5	37.42	0.0071	-3.27	460
Case 2	30.0	43.55	0.0073	-3.60	494

2) FROM CASE 0 TO CASE 2

Table 8 summarizes calculated parameters regarding the zero-power control when Z_u increases from 0 mm to 30 mm. From Table 8, we observe the following features:

- As discussed in Sec. III.B, F_0 increases as the increase of Z_u, whereas k_{linear} almost maintains constant.
- The magnitude of $\partial F/\partial Z_h$ increases as the increase of F_0 [6], [11].
- Since k_{linear} is constant and the magnitude of $\partial F/\partial Z_h$ increases, $\min\left(\partial I/\partial Z_h\right)$ increases as the increase of Z_u.

Hence, the upper magnet enhances F_0 with the price of increasing $\min\left(\partial I/\partial Z_h\right)$.

TABLE 9. Parameters regarding zero-power control during transition from Case 0 to Case 3.

	R_f	F_0	k_{linear}	$\partial F/\partial Z_h$	$\min(\partial I/\partial Z_h)$
Case 0	15.00	9.17	0.0073	-1.43	197
	23.75	28.51	0.0142	-3.54	249
Transition	32.50	45.24	0.0197	-4.26	216
	41.25	53.13	0.0201	-3.71	185
Case 3	50.00	53.60	0.0199	-3.03	152

3) FROM CASE 0 TO CASE 3

Table 9 summarizes calculated parameters regarding the zero-power control when R_f increases from 15 mm to 50 mm. From Table 9, we observe the following features:

- As discussed in Sec. III.B, F_0 and k_{linear} increase as the increase of R_f. However, upper limits are observed for F_0 and k_{linear} at around $R_f = 41.25$ and 32.50mm, respectively. In fact, the two upper limits result from the over-sized floating magnet ($R_f \gg Z_h$ and $R_f \gg R_c$) whose magnetic field near the iron core approaches a constant value so that further enlarging the floating magnet will not enhance F_0 or k_{linear} any more.
- The magnitude of $\partial F/\partial Z_h$ firstly increases as the increase of F_0 [6, 11], and then decreases as the further increase of R_f. Such a decrease in the magnitude of $\partial F/\partial Z_h$ results from the quasi-equal magnetic field nearby the over-sized floating magnet ($R_f \gg Z_h$ and $R_f \gg R_c$).
- For the over-sized floating magnet, since k_{linear} is constant and the magnitude of $\partial F/\partial Z_h$ decreases, $\min\left(\partial I/\partial Z_h\right)$ decreases as the increase of R_f.

Hence, the floating magnet enhances F_0 and reduces $\min\left(\partial I/\partial Z_h\right)$ with a sufficient size ($R_f \gg Z_h$ & $R_f \gg R_c$).

4) SUMMARY

Tables 10 summarizes the influences on the zero-power control by the three geometric modifications. Technically, the zero-power control prefers larger F_0 and smaller $\min\left(\partial I/\partial Z_h\right)$.

TABLE 10. Influences on zero-power control by geometric modifications.

Modification	F_0	k_{linear}	$\lvert\partial F/\partial Z_h\rvert$	$\min(\partial I/\partial Z_h)$
Increasing R_e	↗	↗	↗	↘
Increasing Z_u	↗	→	↗	↗
Increasing R_f	↗→	↗→	↗↘	↗↘

IV. CONCLUSION

This work analyzes the zero-power maglev system by comparing three geometric modifications, including the core extension, the upper permanent magnet and the floating permanent magnet. Four target cases are numerically solved and analyzed. In order to enhance the zero-power force and reduce the controller-gain requirement, the maglev system should adopt the core extension and enlarge the floating magnet sufficiently. On the contrary, the maglev system should remove any permanent magnet from the electromagnet, because the upper magnet not only greatly accelerates the saturation of the iron core but also significantly increases the controller-gain requirement. The concluding remarks in this work may also provide insights for the PEMS technology, e.g. to insert the permanent magnet into the guide-way rather than the iron core.

CONFLICTS OF INTEREST

The authors declare no conflict of interest.

REFERENCES

[1] H.-W. Lee, K.-C. Kim, and J. Lee, "Review of maglev train technologies," *IEEE Trans. Magn.*, vol. 42, no. 7, pp. 1917–1925, Jul. 2006, doi: 10.1109/Access.2019.2939879.
[2] K. Oguchi and Y. Tomigashi, "Digital control for a magnetic suspension system as an undergraduate project," *Int. J. Electr. Eng. Edu.*, vol. 27, no. 3, pp. 226–236, Jul. 1990, doi: 10.1177/002072099002700305.
[3] D. Cho, Y. Kato, and D. Spilman, "Sliding mode and classical controllers in magnetic levitation systems," *IEEE Control Syst. Mag.*, vol. 13, no. 1, pp. 42–48, Feb. 1993, 10.1109/37.184792.
[4] W. Barie and J. Chiasson, "Linear and nonlinear state-space controllers for magnetic levitation," *Int. J. Syst. Sci.*, vol. 27, no. 11, pp. 1153–1163, Nov. 1996, doi: 10.1080/00207729608929322.
[5] T. H. Wong, "Design of a magnetic levitation control system-an undergraduate project," *IEEE Trans. Educ.*, vol. TE-29, no. 4, pp. 196–200, Nov. 1986, doi: 10.1109/TE.1986.5570565.
[6] W. G. Hurley and W. H. Wolfle, "Electromagnetic design of a magnetic suspension system," *IEEE Trans. Educ.*, vol. 40, no. 2, pp. 124–130, May 1997, doi: 10.1109/13.572325.
[7] A. El Hajjaji and M. Ouladsine, "Modeling and nonlinear control of magnetic levitation systems," *IEEE Trans. Ind. Electron.*, vol. 48, no. 4, pp. 831–838, Aug. 2001, doi: 10.1109/41.937416.
[8] W. Yu and X. O. Li, "A magnetic levitation system for advanced control education," in *Proc. 19th IFAC World Congr.*, Cape Town, South Africa, 2014, pp. 9032–9037.
[9] J. J. Hernández-Casañas, M. A. Márquez-Vera, and B. D. Balderrama-Hernández, "Characterization and adaptive fuzzy model reference control for a magnetic levitation system," *Alexandria Eng. J.*, vol. 55, no. 3, pp. 2597–2607, Sep. 2016, doi: 10.1016/j.aej.2016.04.032.
[10] K. H. Lundberg, K. A. Lilienkamp, and G. Marsden, "Low-cost magnetic levitation project kits," *IEEE Control Syst. Mag.*, vol. 24, no. 5, pp. 65–69, Oct. 2004, doi: 10.1109/MCS.2004.1337863.
[11] M. G. Yoon and J. H. Moon, "A simple analog controller for a magnetic levitation kit," *Int. J. Eng. Res. Technol.*, vol. 5, no. 3, pp. 94–97, Mar. 2016.
[12] Googol Technology. (2018). Shenzhen, China. *Magnetic Levitation System GML2001*. [Online]. Available: http://www.googoltech.com/pro_view-67.html
[13] T. C. Wang and Y.-K. Tzeng, "A new electromagnetic levitation system for rapid transit and high speed transportation," *IEEE Trans. Magn.*, vol. 30, no. 6, pp. 4734–4736, Dec. 1994, doi: 10.1109/20.334205.
[14] Z. Zhang, C. Shang, L. She, W. Chang, and L. Zhang, "Structural optimal design of a permanent-electro magnetic suspension magnet for middle-low-speed maglev trains," *IET Electr. Syst. Transp.*, vol. 1, no. 2, pp. 61–68, Jun. 2011.
[15] T. Gao, J. Yang, L. Jia, Y. Deng, W. Zhang, and Z. Zhang, "Design of new energy-efficient permanent magnetic maglev vehicle suspension system," *IEEE Access*, vol. 7, pp. 135917–135932, Sep. 2019, doi: 10.1109/Access.2019.2939879.

ZEYI ZHANG received the bachelor's and Ph.D. degrees from the University of Hong Kong, in 2014 and 2018, respectively. He is currently a Lecturer with the Institute of Permanent Maglev and Railway Technology (IPMRT), Jiangxi University of Science and Technology. His research interest includes permanent maglev and automatic control.

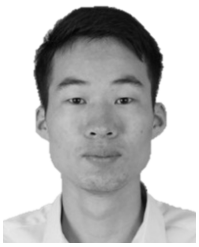

TAO GAO received the bachelor's degree from Zhengzhou University, in 2016. He is currently pursuing the Ph.D. degree with the Jiangxi University of Science and Technology. His main research direction is maglev train control technology. One of the researchers in the rainbow rail system.

YAO QIN received the bachelor's degree from the Jiangxi University of Science and Technology, in 2020, where he is currently pursuing the master's degree. His research interests include maglev train control technology and the integrated maglev train control systems.

JIE YANG was born in Anhui, China, in 1979. He received the Ph.D. degree in rail traffic safety from the State Key Laboratory of Rail Traffic Control and Safety, Beijing Jiaotong University, China, in 2017. He joined the Jiangxi University of Science and Technology, as the Director of the Institute of Permanent Maglev and Railway Technology (IPMRT). His current research interests include permanent maglev and energy-efficient train control.

FAZHU ZHOU was born in Hainan, China, in 1986. He received the bachelor's degree from the Jiangxi University of Science and Technology, in 2009, where he is currently pursuing the Master's degree. His research interests include maglev train control technology and the rainbow rail systems.